Delft University of Technology

Document Version
Final published version

Licence
CC BY

Citation (APA)
van Valderen, R. D., Juarez-Garza, B. E., de Smit, S., Ottens, M., & Haringa, C. (2026). CFD–DEM characterization of a 250 mL stirred-tank bioreactor for shear-sensitive stem cell microcarrier cultures. *Biochemical Engineering Journal*, *236*, Article 110365. https://doi.org/10.1016/j.bej.2026.110365

Important note
To cite this publication, please use the final published version (if applicable).
Please check the document version above.

Copyright
In case the licence states “Dutch Copyright Act (Article 25fa)”, this publication was made available Green Open Access via the TU Delft Institutional Repository pursuant to Dutch Copyright Act (Article 25fa, the Taverne amendment). This provision does not affect copyright ownership.
Unless copyright is transferred by contract or statute, it remains with the copyright holder.

Sharing and reuse
Other than for strictly personal use, it is not permitted to download, forward or distribute the text or part of it, without the consent of the author(s) and/or copyright holder(s), unless the work is under an open content license such as Creative Commons.

Takedown policy
Please contact us and provide details if you believe this document breaches copyrights.
We will remove access to the work immediately and investigate your claim.

This work is downloaded from Delft University of Technology.

Biochemical Engineering Journal 236 (2026) 110365

Contents lists available at ScienceDirect

Biochemical Engineering Journal

journal homepage: www.elsevier.com/locate/bej

Regular Article

CFD–DEM characterization of a 250 mL stirred-tank bioreactor for shear-sensitive stem cell microcarrier cultures

Ramon D. van Valderen, Brenda E. Juarez-Garza, Stijn de Smit, Marcel Ottens, Cees Haringa *

Delft University of Technology, Van Der Maasweg 9, Delft, 2629 HZ, Zuid-Holland, The Netherlands

ARTICLE INFO

Dataset link: 10.4121/2a82e089-a272-47be-8043-d505dba03339

Keywords:
Computational fluid dynamics
Discrete element method
Large eddy simulations
Stem cell cultures
Microcarriers
Hydrodynamic stress
Scale-up

ABSTRACT

Human stem cells hold great potential for creating curative therapies for various different diseases. Producing clinically relevant number of stem cells requires controllable and scalable systems such as stirred-tank bioreactors. Fortunately, recent advances in 3D cultivation protocols, such as the use of microcarriers, have enabled the expansion and differentiation of stem cells as suspension cultures. To make a stem cell bioreactor process scalable, it is critical to understand how the operating conditions influence bioreactor scale-up parameters, microcarrier suspension, and hydrodynamic stresses experienced by the stem cells. We present a comprehensive computational fluid dynamics and discrete element method (CFD–DEM) model of microcarrier cultures in a 250 mL stirred-tank bioreactor. We validated our model using literature and experimental data and showed that our model predicted important engineering parameters, like power input, mixing time, free surface $k_L a$, and microcarrier just-suspension stirring speed, within 20% accuracy over a wide range of operating conditions. Based on the experimental and numerical data, the results indicated that down-pumping at 90 rpm was the preferred operational mode to reach sufficient microcarrier suspension while minimizing hydrodynamic stress from a microcarrier lifeline perspective. This validated CFD–DEM modeling approach provides a basis for identifying suitable operating conditions across stirred-tank bioreactor scales, thereby supporting the process development and rational scale-up of stem cell-based therapies.

1. Introduction

Human stem cells have emerged as a promising platform for regenerative medicine, enabling applications such as cell therapy, tissue engineering, and creation of bioartificial organs [1]. For example, mesenchymal stem cells (MSCs) are classified as multipotent and can differentiate into osteoblasts, adipocytes, and chondrocytes [2]. MSCs therefore have great therapeutic potential to treat various neurodegenerative diseases, as well as other inflammatory diseases [2,3]. More recently, the use of human inducible pluripotent stem cells (hiPSCs) gained popularity due to their pluripotency and self-renewal capacity, giving hiPSCs therapeutic potential to tackle various illnesses such as Parkinson's disease, cancer, and sickle cell disease [4,5].

To produce clinically relevant numbers of stem cells, expansion and differentiation protocols are needed in controllable and scalable systems [6]. Typically, to cultivate stem cells in suspension, microcarriers are used to provide the necessary surface on which the stem cells can grow [3,7]. This enabled cultivation in stirred-tank bioreactors, which are known for their scalability and ability to tightly control critical process variables such as pH, temperature and dissolved oxygen concentration [6,8]. MSCs have already been successfully cultivated in stirred-tank bioreactors using microcarriers [7,9]. Similarly, Teale et al. [10] demonstrated successful hiPSCs expansions on microcarriers in lab-scale stirred tank bioreactors. Moreover, EBs have recently been combined with microcarriers in a new approach to support formation of hematopoietic organoids in suspension, where the addition of microcarriers to which EBs attach was found critical to increase the production of red blood cells directly from hiPSCs [11,12].

These developments in 3D stem cell cultivation protocols — whether through self-organizing aggregates, adherent growth on microcarriers, or a combination thereof — enabled growth as suspension cultures in (stirred-tank) bioreactor systems. However, in a stirred-tank bioreactor a balance must be found between agitation-induced hydrodynamic stress and suspension of microcarriers or stem cell aggregates, while maintaining sufficient oxygen transfer and nutrient mixing. Properly understanding and tuning the local hydrodynamic conditions inside the bioreactor is critical to maintain cell viability [13,14], prevent necrotic core formation inside aggregates [15,16], and ensure full microcarrier

* Corresponding author.
E-mail address: c.haringa@tudelft.nl (C. Haringa).

https://doi.org/10.1016/j.bej.2026.110365
Received 16 June 2026; Received in revised form 31 July 2026; Accepted 11 August 2026
Available online 18 August 2026
1369-703X/© 2026 The Author(s). Published by Elsevier B.V. This is an open access article under the CC BY license (http://creativecommons.org/licenses/by/4.0/).

and aggregate suspension while minimizing hydrodynamic stress [9,10].

Computational fluid dynamics (CFD) has become an important tool in bioprocess engineering to characterize bioreactors in terms of the impeller power number, mixing efficiency, and interfacial mass transfer [17–19]. More specifically in the context of shear-sensitive cells, single-phase CFD has been used to quantify hydrodynamic stresses inside culture vessels [20–23]. Multiphase CFD studies on microcarrier-laden flows in bioreactors have also been performed using Eulerian–Eulerian (E-E) approaches, which enables investigation of microcarrier suspension and dispersion behavior [24–26]. However, a limitation of both single-phase and E-E CFD approaches is that microcarriers are not tracked individually, even though the importance of accounting for the hydrodynamic stress exposure from the perspective of the microcarrier (lifelines [27]) has been acknowledged [28,29].

Furthermore, many stem cell cultivations in agitated bioreactors rely dissolved oxygen (DO) control via only headspace aeration [9,10,30], to avoid hydrodynamic stress through bubble bursting [31–33]. However, bioreactor batch sizes for allogeneic cell therapies have been projected to reach between 200 and 2000 L to accommodate the required number of cells per product per year [34,35], and controlling the DO only via headspace aeration might not be feasible. Quantifying the headspace free-surface volumetric oxygen mass transfer coefficient (k_La), alongside other scale-up parameters such as impeller power number (Po), volumetric power input (P/V), and mixing time (t_{95}), is critical for understanding oxygen transfer limitations at larger scales and for the rational design and scale-up of stirred-tank bioreactor protocols for shear-sensitive stem cell cultures [36]

In this work, we present a comprehensive Euler–Lagrangian (E-L) CFD–DEM model to quantify bioreactor scale-up parameters, microcarrier suspension and hydrodynamic stresses in one combined model of a 250 mL bioreactor. Microcarriers are modeled as individual particles using an unresolved discrete element method (DEM) approach, which enables tracking of microcarrier suspension and hydrodynamic stresses on a per-particle basis. We validate this model against a range of experimental data, both from literature and our own experiments, including mixing time, free surface k_La, and particle suspension measurements. Once validated, we investigate how bioreactor operating parameters — including stirring speed, impeller pumping mode, impeller height, and filling volume — influence the bioreactor performance. Bioreactor performance is determined by quantifying important scale-up parameters such as $\frac{P}{V}$, t_{95}, and free surface k_La. Furthermore, microcarrier suspension, dispersion, and hydrodynamic stresses experienced by the microcarriers are quantified directly from the microcarrier lifelines. Although this work is centered around microcarriers, we believe our model can be translated relatively easily to systems with stem cell aggregates, like EBs, upon determination of their size and density. To conclude, we discuss how to improve the model's accuracy and the implications of using detailed CFD–DEM models to support process scale-up of shear-sensitive stem cell microcarrier cultures.

2. Material and methods

2.1. Bioreactor configuration

The Applikon MiniBio 250 mL (Getinge, Delft, The Netherlands) was used in a typical mammalian cell culture configuration (Fig. 1). This includes one or two elephant ear impellers with a blade angle of 45°. The vessel was equipped with a temperature sensor, dissolved oxygen sensor, pH sensor, open-hole sparger, and two sampling tubes. The bioreactor dimensions are listed in Table 1.

Table 1
Dimensions and geometric ratio's of Applikon MiniBio 250 mL.

Parameter	Symbol	Value	Unit
Tank diameter	T	0.06	m
Impeller diameter	D	0.028	m
Tank height	H	0.115	m
Off-bottom clearance	C	0.016–0.026	m
Inter-impeller distance	S	0.028–0.042	m
(–)	D/T	0.467	–
(–)	H/T	1.91	–
(–)	C/D	1.08–1.75	–
(–)	S/D	1–1.5	–

2.2. Numerical simulations

2.2.1. Fluid flow

M-Star CFD software v3.13.124 was used to simulate the two-phase fluid flow, which uses the Lattice-Boltzmann (LB) method to solve the incompressible Navier–Stokes equations:

$$\nabla \cdot u = 0, \tag{1}$$

$$\frac{\partial u}{\partial t} + (u \cdot \nabla)u = -\frac{\nabla p}{\rho_f} + \nu\nabla^2 u + g + \frac{1}{\rho_f} f_s + \frac{1}{\rho_f} f_{ext}. \tag{2}$$

Here, the local fluid velocity at time t is described by u, the gravitational acceleration by g, the pressure by p, the fluid density by ρ_f, the fluid kinematic viscosity by ν, the surface tension force density by f_s, and any external forces acting on the fluid by f_{ext}. The software numerically solves the lattice Boltzmann equation:

$$f_i(x + c_i\Delta t, t + \Delta t) = f_i(x, t) + \Omega_i(x, t). \tag{3}$$

Eq. (3) represents the fluid by a set of discrete velocity distribution functions $f_i(x,t)$, which move with velocity c_i to a neighboring lattice point $x + c_i\Delta t$ at the next time step $t + \Delta t$, which is called the streaming step. At the same time, particles are redistributed among the populations f_i during the collision step via the simplified Bhatnagar–Gross–Krook (BGK) collision operator $\Omega_i(x,t)$ [37].

To model the free surface dynamics, M-Star uses a conservative phase-field lattice Boltzmann method based on the Allen–Cahn equation [38,39]. The density of the system is described by

$$\rho = \rho_f \cdot \phi, \tag{4}$$

where ρ_f is the density of the fluid and ϕ is an order parameter that defines the volume fraction of the fluid. The gas–liquid interface is described by the spatio-temporal evolution of ϕ using

$$\frac{\partial \phi}{\partial t} + \nabla \cdot \phi u = \nabla \cdot \left[M \left(\nabla\phi - \frac{1 - 4(\phi - \frac{1}{2})^2}{W} \right) n \right], \tag{5}$$

where M is the mobility parameter, W the interface width and n the normal vector. In typical bioreactor processes the density of the liquid is order-of-magnitudes larger than the density of the gas occupying the headspace ($\rho_l/\rho_g \approx 1000$). The gas dynamics can therefore be simplified and modeled implicitly by assuming a constant pressure (1 atm) along the gas–liquid interface [36].

We used large-eddy simulation (LES) with the Smagorinsky–Lilly closure model [40]. This model defines the local turbulent viscosity ν_t by

$$\nu_t = (C_s\Delta x)^2 \|S\|, \tag{6}$$

where Δx is the lattice spacing, $\|S\|$ the norm of the resolved strain rate tensor and C_s the Smagorinsky coefficient. We set C_s to 0.1 based on prior direct numerical simulations and other validated LB-LES bioreactor simulations [27,40,41]. The energy dissipation rate ε was calculated by

$$\varepsilon = 2(\nu + \nu_t)\|S\|^2. \tag{7}$$

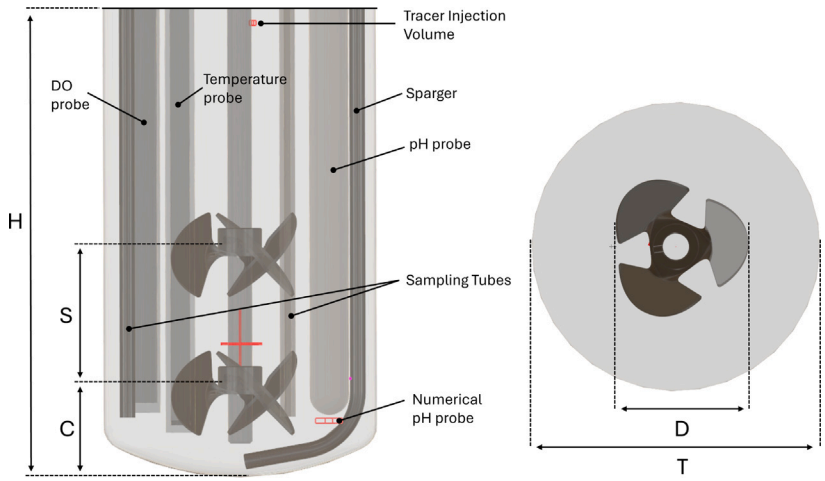


Fig. 1. Applikon MiniBio 250 mL reactor geometry.

The immersed boundary method was used to model the impeller–fluid interactions [42]. The impeller power input P was calculated by integrating the impeller torque τ over the entire surface area of the impeller and shaft assembly [43]. The impeller Power Number Po was then determined by

$$Po = \frac{\tau\omega}{\rho_f N^3 D^5}, \tag{8}$$

where ω is the angular velocity, N the impeller speed, and D the impeller diameter.

The power number was evaluated with respect to the impeller Reynolds number Re_{imp}, which is defined as

$$Re_{imp} = \frac{N D^2}{\nu}. \tag{9}$$

2.2.2. Scalar transport mixing time

Numerical mixing studies were conducted using the scalar transport model which describes the passive transport of a scalar through the fluid via the advection–diffusion equation:

$$\frac{\partial c}{\partial t} = \nabla(D_m \cdot \nabla c) - \nabla(u \cdot c). \tag{10}$$

Here, D_m is the molecular diffusion coefficient and c the scalar concentration field. To maintain consistency with the experimental pH tracer method (Section 2.6.1), the concentration of a fictive tracer was monitored during a simulation in a cuboid of $5 \times 10 \times 5$ lattice points (x, y, z respectively) below the pH probe (Fig. 1).

The tracer was pulse injected below the liquid surface once the mean fluid kinetic energy reached a pseudo-steady state, ensuring a fully developed flow field. In total, six fictive tracers were injected consecutively with a 2 s interval to quantify the uncertainty in the mixing time during the large eddy simulations [44]. The fictive tracer was assumed to have a diffusion coefficient of $9.3 \cdot 10^{-9}$ m^2/s similar to H^+ in water [45].

2.2.3. Free surface volumetric oxygen mass transfer coefficient (k_La) model

The free surface k_La was obtained from the computed free surface interfacial area A and the free surface velocity V_f. The free surface velocity is related to the liquid-side mass transfer coefficient k_L through the following non-dimensional groupings [36]:

$$\left(\frac{k_L L}{D_m}\right) = C\left(\frac{V_f L}{\nu}\right)^a \left(\frac{\nu}{D_m}\right)^b, \tag{11}$$

where D_m is the oxygen diffusion coefficient and L the characteristic length scale which was set to the diameter of the bioreactor. The values for a, b and C were set to 4/5, 1/3 and 0.21 respectively based on prior literature [36,46]. The oxygen diffusion coefficient in water at 37 °C was assumed to be $2.56 \cdot 10^{-9}$ m^2/s [47].

2.3. Particle model

Particles were modeled in tandem to the fluid using the discrete element method (DEM). The particle trajectories are described via Newton's second law

$$m_i \frac{v_i}{dt} = F_i^g + F_i^{f\to p} + F_i^{p\to p}, \tag{12}$$

where m_i is the particle mass, v_i the particle velocity, F_i^g is the gravity force, $F_i^{f\to p}$ the fluid forces acting on the particle, and $F_i^{p\to p}$ particle–particle interaction forces. The fluid–particle force $F_i^{f\to p}$ was defined as

$$F_i^{f\to p} = F_i^b + F_i^d + F_i^{vm}, \tag{13}$$

where F_i^b is the buoyancy force, F_i^d the drag force and F_i^{vm} the virtual mass force. For the drag coefficient C_D the analytical representation from Brown and Lawler [48] was used:

$$C_D = \frac{24}{Re_p}(1 + 0.15 Re_p^{0.681}) + \frac{0.407}{1 + \frac{8710}{Re_p}}. \tag{14}$$

This drag coefficient equation is valid up until $Re_p < 10^5$. The particle Reynolds number Re_p is defined by

$$Re_p = \frac{\rho_f d_p \|u - v\|_2}{\mu}, \tag{15}$$

where $\|u - v\|_2$ is the Euclidean norm of the particle slip velocity.

We recognize that the general equation of particle motion (Eqs. (12), (13)) might include additional forces such as lift forces, the pressure gradient force, the Basset history force and lubrication forces [49]. Lacking any quantitative particle trajectory validation data, and to maintain computational efficiency, we only included the gravity-buoyancy, drag and virtual mass forces as done previously [43,50].

A soft-sphere contact model was used to model the particle–particle contact force ($\mathbf{f}_{ij}$) using a standard Hertzian model for the normal force and a Mindlin model for the tangential force [51]. These models were combined to link the stiffnesses and the damping coefficients to the physical properties of the particles described by the Young's modulus (Y), the Poisson ratio (ν_p), and the coefficient of restitution (e_r) (Supplementary data Table S1).

The effect of the particle motion on a fluid voxel (2-way coupling) was modeled with a simplified density approach, which only considered the net effect of the gravity and buoyancy forces:

$$F^{p\to f} = F^g + F^b = N_p V_p (\rho_p - \rho_f). \tag{16}$$

Here, N_p is the number of particles in a fluid voxel and V_p the volume of the particle. Likely, the above coupling formulation underestimates the particle–fluid force as drag and virtual mass forces are

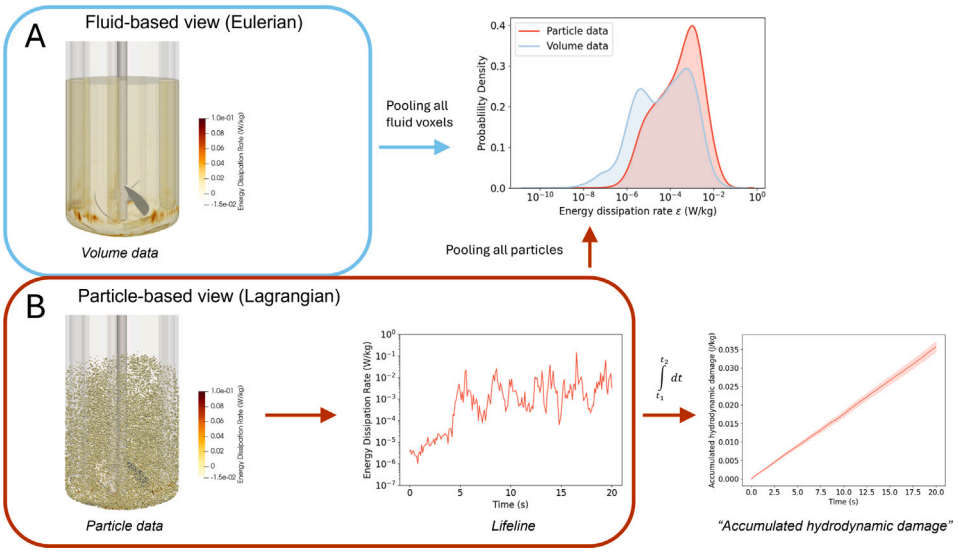


Fig. 2. Fluid-based vs particle-based perspectives on hydrodynamic stress. Energy dissipation rate (ε) distribution obtained from the Eulerian fluid (A) and from the Lagrangian microcarrier perspective (B). The ε-distribution derived from particle lifelines inherently accounts for the particle residence time distribution inside the bioreactor, resulting in significantly different ε-distribution when obtained from the fluid directly. Time-integration of ε lifelines yields a metric that represents the amount of Accumulated Hydrodynamic Damage.

non-negligible. However, we found that the two-way coupling through Newton's third law resulted in numerically unstable simulations. Based on our particle suspension experiments (Section 3.1.3), including the density-based two-coupling improved the predicted size of the settled particle bed on the bioreactor bottom, compared to completely neglecting $F^{p\rightarrow f}$ (1-way coupling) (Supplementary data Figure S1).

2.4. Lagrangian metrics for bioreactor performance

2.4.1. Lagrangian-based hydrodynamic stress

We exploit the Lagrangian nature of our CFD–DEM model to obtain energy dissipation rate (ε) distributions directly from microcarrier lifelines (Fig. 2). We use ε as a proxy for hydrodynamic stress, as this accounts inherently for both the resolved and unresolved scales during the simulations [52]. The Kolmogorov length scale λ_k is then computed from ε, which is defined as:

$$\lambda_k = (\frac{\nu^3}{\varepsilon})^{1/4}, \tag{17}$$

where ν is the fluid kinematic viscosity. The λ_k distribution was constructed from 60 s of Lagrangian particle data, after the flow had reached pseudo-steady state ($t > t_{mix}$).

The Lagrangian microcarrier lifelines also contain a transient component, where the ε observed by the microcarrier (ε_p) can be tracked through time. The ε_p lifelines where then integrated using

$$AHD_p = \int_{t_1}^{t^2} \varepsilon_p(t)dt. \tag{18}$$

This provides an alternative perspective on how much hydrodynamic stress a microcarrier accumulates over time, which we have named Accumulated Hydrodynamic Stress (ADH_p) similar to the work of Anand et al. [53]. The microcarrier lifelines were sampled every 0.1 s and the $\varepsilon_p(t)$ were integrated using a composite trapezoidal rule.

2.4.2. Lagrangian-based suspension and homogenization criteria

We propose a method for tracking the suspension on a per-particle basis, similar to how Zwietering [54] defined N_{js}. We define a particle p_i to be on the reactor bottom if

1. $p_{i,y} < 6.2$ mm, meaning that the particle height is below the impeller shaft and thus inside the dish reactor bottom
2. and either
   (a) p_i is inside the fluid voxel closest to the vessel wall (wall distance <= Δx)
   (b) p_i overlaps with another particle p_j that is itself on the reactor bottom

Particles are considered overlapping when

$$\|p_i - p_j\| <= r_i + r_j, \tag{19}$$

where $\|p_i - p_j\|$ is the distance between the particle center points and r_i and r_j the particle radii. This definition allows particles stacked on top of vessel-adjacent particles to be classified as on the reactor bottom (Supplementary data Figure S7). A particle p_i is then considered suspended if p_i spends less than 2 s on the reactor bottom, analog to the Zwietering [54] definition. Although this Lagrangian suspension definition still requires arbitrary thresholds (e.g., bottom distance and maximum residence time), it quantifies the suspended particle fraction, allowing a sufficient suspension speed (N_{ss}) to be defined. Unlike N_{js}, it recognizes that a small fraction of unsuspended particles (e.g., 2%) may be acceptable [55]. Rather than replacing N_{js}, it provides a complementary measure of the actual fraction of particles in suspension.

The degree of microcarrier dispersion is evaluated using the mean nearest neighbor separation distance $\bar{r}_{nn}$:

$$\bar{r}_{nn} = \frac{1}{N_p}\sum_n r_{nn}, \tag{20}$$

where r_{nn} is the distance of a particle to its nearest neighbor and N_p is the total number of particles. $\bar{r}_{nn}$ will increase if the particles are dispersed more homogeneously, and can therefore be used to compare different bioreactor operational conditions, as long as the concentration of particles remains constant (Supplementary data Figure S8).

2.5. Physical and numerical parameters

The physical and numerical parameters used for the CFD–DEM simulations are listed in Table 2. All boundaries were set to interpolated half-way bounce-back boundaries. No-slip boundary conditions were used for fluid-vessel and fluid-probe interactions. Only for the liquid free surface a free-slip boundary condition was used. We found that

Table 2
Physical and numerical parameters used during the CFD–DEM simulations.

Parameter	Symbol	Value	Unit
Fluid density	ρ_f	993	kg/m^3
Fluid kinematic viscosity	ν_f	$6.96 \cdot 10^{-7}$	m^2/s
Surface tension	σ	0.07025	N/m
CFD lattice size	Δx	224	µm
Number of Cospheric particles	$N_{p,\,Cospheric}$	33 000	–
Cospheric particles density	$\rho_{p,\,Cospheric}$	1030	kg/m^3
Cospheric particles size	$d_{p,\,Cospheric}$	180–212 (Uniform distributed)	µm
Number of Cytodex-1 microcarriers (0.5 g/L)	$N_{p,\,Cytodex-1}$	400,000 – 600,000	–
Cytodex-1 particle density	$\rho_{p,\,Cytodex-1}$	1030	kg/m^3
Cytodex-1 particle size	$d_{p,\,Cytodex-1}$	150–180 (Uniform distributed)	µm
Young's modulus	Y	1	MPa
Poisson's ratio	ν_p	0.3	–
Restitution coeff.	e_p	0.1	–
Sliding friction coeff.	μ_p	0.5	–
gravitational constant	g	9.81	m/s^2

250 lattice points across the bioreactor diameter (≈ 113 lattice points across impeller diameter) with a Courant number of 0.05 was optimal in terms of simulation accuracy and grid convergence (Supplementary data Figure S2). The grid dependence study was only conducted with respect to global quantities (i.e., Po and t_{mix}), and not regarding the Lagrangian metrics. Refining the grid beyond 250 lattice points ($\Delta x \approx$ 224 µm) would result in $d_p > \Delta x$, which would violate the assumptions of unresolved DEM particles and introduce numerical ambiguity on how to treat particles larger than the fluid cells. Although various numerical approaches exist to deal with $d_p \gtrapprox x$ (e.g., Pirker et al. [56]), such methods are not supported in M-Star CFD 3.13.124. Consequently, the grid dependency of the Lagrangian metrics could not be fully assessed. We acknowledge this limitation, and future work should evaluate the sensitivity of these Lagrangian metrics using methods that permit further grid refinement while maintaining a consistent fluid–particle coupling.

Lacking any quantitative information on the DEM parameters for suspended microcarriers, we chose initial DEM parameters based on the work of Nijssen et al. [49] on fluidized beds with relative comparable fluid and particle properties. We then adjusted the DEM parameters based on our particle suspension experiments and based on computational efficiency, resulting in the parameters listed in Table 2. The DEM time step size was set using Eq. S3 (Supplementary data), resulting in approximately 20 DEM sub-cycles per fluid timestep. A standard D3Q19 velocity discretization was used and simulations were performed on a standard desktop containing an NVIDIA RTX3090 24 GB GPU. Further numerical details are described in the Supplementary data Section S1.1.

2.6. Experiments

2.6.1. Mixing time determination

The bioreactor mixing time was determined using the pH tracer method where the H^+ concentration is monitored using a pH probe until it reached within ±5% of its final stable concentration (t_{95}). Mixing times were measured in triplicate using an AppliSens pH probe (Getinge, Delft, The Netherlands). The response time of our pH probe ($t_{probe,90}$) was measured to be 55.0 ± 20.4 s (Supplementary data Figure S3). This is in the same order of magnitude as the measured bioreactor mixing time of 10 – 20 s and can therefore not be neglected. The pH probe lag correction method proposed by Zhang et al. [57] was used to deconvolute our measured pH signal and determine the true mixing times. We refer to Supplementary data Section S5 for the details on the mixing time experiments and signal deconvolution procedure. Furthermore, mixing time results were compared to the empirical correlation of van 't Riet and van der Lans [58] (Supplementary data Equation S1).

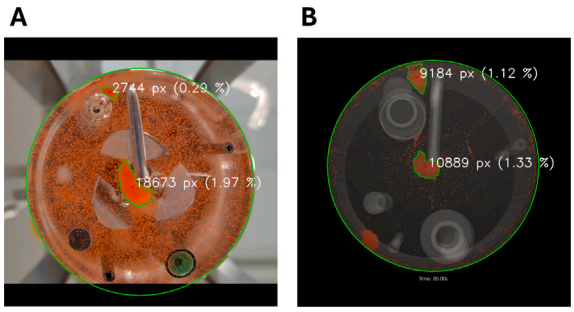


Fig. 3. Example of image analysis workflow to determine the relative size of the settled particle beds during experiments (A) and simulations (B).

2.6.2. Free surface k_La determination

The headspace aerated free surface k_La was measured using the gassing out method [59], as further explained in Supplementary data Section S6. The k_La coefficients were measured in triplicate at 37 °C using regular tap water was as medium and the impeller in down-pumping mode. The DO concentration was measured with a LumiSens Optical dO_2 Sensor (Getinge Applikon, Delft, The Netherlands) and the measurements were automated using Lucullus (Securecell AG, Urdorf, Switzerland).

2.6.3. Particle suspension experiments

Polyethylene particles with a density of 1030 kg/m^3 and diameter between 180 and 212 µm (Cospheric, Somis, United States) were used for the particle suspension experiments, as model particles for the commonly used microcarrier Cytodex-1 [12]. In total, approximately 33000 particles were added (0.17 g) to the bioreactor filled with 160 mL demineralized water, in the presence of 20 µL of Tween20 (Merck KGaA, Darmstadt, Germany), and operated with a single impeller. Images of the bioreactor bottom were taken to capture the size and shape of the settled particle bed. For each condition, 3 images were taken with a 5 s interval after the particle suspension reached a quasi-steady state, which were subsequently analyzed using image segmentation (Fig. 3). Nearly identical reactor bottom images were generated for the simulations where the size of the settled particle bed was quantified using the number of pixels confining the area identified as the settled particle bed, according to the image processing workflow described in Supplementary data Section S8. The particle bed size was normalized by the number of pixels confining the area of the bioreactor bottom. The obtained N_{js} values from the experiments were compared to predictions of the empirical correlation of Loubière et al. [26] (Supplementary data Equation S2).

3. Results and discussion

3.1. Model validation

3.1.1. Hydrodynamic validation

The predicted power number of the CFD–DEM simulations were compared to the experimental results of Zhu et al. [60] and Delbridge et al. [18], who both used elephant ear impellers with similar $\frac{D}{T}$ and $\frac{C}{T}$ ratios. The predicted power numbers closely follow the reference power numbers across the investigated impeller Reynolds numbers (Fig. 4B). This includes the expected increase of the power number in the transitional flow regime for Newtonian fluids [61]. At the fully turbulent regime ($Re_{imp} > 2 \cdot 10^4$ [61]) the simulated power number Po converges to 1.90 ± 0.01, which is in alignment with the power number data of Zhu et al. [60] at 2.12 ± 0.26 and data of Delbridge et al. [18] at 2.13 ± 0.01. Small deviations in the power number were expected between our system, and the systems of Zhu et al. [60] and Delbridge

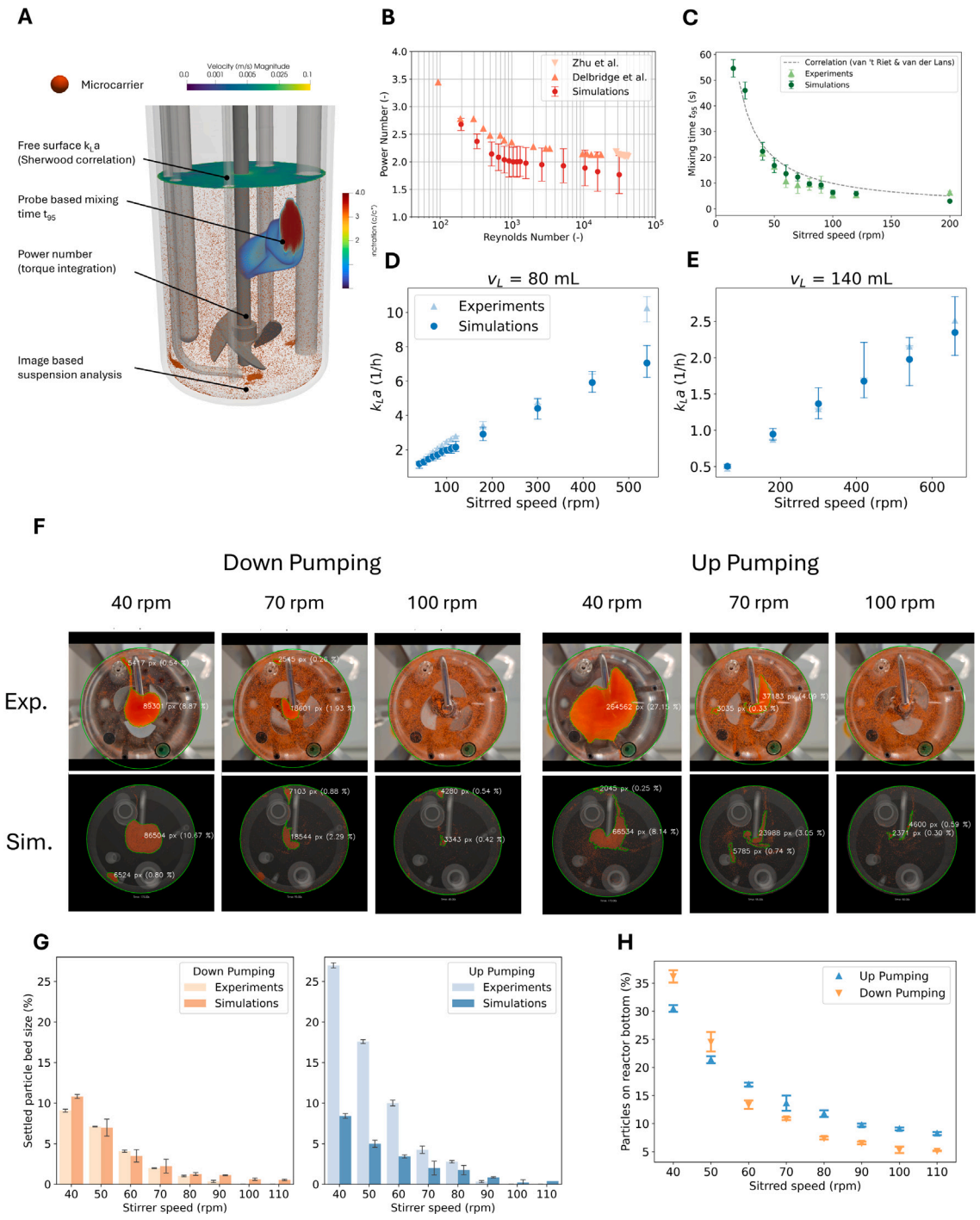


Fig. 4. Validation of CFD–DEM model the Applikon MiniBio 250 mL for shear-sensitive microcarrier cultures. (A) Schematic overview of parameters which were extracted from CFD–DEM model and compared to experimental data, including power number P_o, mixing time t_{95}, free surface k_La, and image based particle suspension experiment. (B) Comparison of simulated power number with data from Zhu et al. [60] and Delbridge et al. [18] for a single down-pumping elephant ear impeller. (C) Comparison of simulated and experimental mixing times t_{95} using the pH tracer method, with additional comparison to the empirical mixing time correlation of van 't Riet and van der Lans [58]. (D) Comparison of simulated free surface k_La at V_L = 80 mL and (E) V_L = 140 mL with experimentally measured k_La using the gassing out method. (F) Visual comparison of simulated and experimental settled particle bed sizes on the bioreactor bottom. Images of the reactor bottom (both simulated and experimental) were subjected to image segmentation to quantify the size of the settled particle bed on the reactor bottom based on the number of pixels inside the identified segmented settled particle bed. (G) simulated and experimental settled particle bed sizes were quantitatively compared for both down-pumping (left) and up-pumping (right). (H) Relative number of particles on bioreactor bottom during simulations as function of stirrer speed.

et al. [18], as the power number is also dependent on the geometry of the vessel and bioreactor internals.

Mixing time experiments were conducted with the pH tracer method and probe lag correction method proposed by Zhang et al. [57]. The simulated mixing times closely follow the measured mixing times across the measured range of stirring speeds, with a mean absolute error of 1.4 s (16.3% relative error) (Fig. 4C). This error is within the average experimental standard deviation of 2.1 s (relative standard deviation of 21.6%). At 200 rpm the limit of the probe lag correction method is reached, as the mixing time ($\approx 5s$) becomes an order of magnitude smaller than the measured $t_{probe,90}$ of 55 ± 20.4 s. Furthermore, we note that our pH probe lag correction might have overcorrected the measured mixing times, as the probe response time measurements were performed under static fluid conditions whereas the mixing times were

measured under dynamic fluid conditions. Although still a good agreement between experimental and simulated mixing times was obtained, for future work we recommend using a different type of probe with a lower response time, such as a conductivity probe [57], to avoid introducing additional inaccuracies via lag time correction methods.

We compared the mixing times to a generic mixing time correlation from van 't Riet and van der Lans [58] (Fig. 4C). This correlation captures the dependency of the mixing time on the stirrer speed correctly, but overestimates the experimental mixing times with a mean absolute error of 3.4 s (39% relative error). This revalidates the usefulness of this correlation to obtain an order-of-magnitude estimation of the mixing times, especially when considering that this correlation was designed for Rusthon impellers and much larger volumes ($> 100L$). However, the accuracy of the CFD model is appealing when the process requires careful design of the operating conditions.

3.1.2. Free surface k_La validation

The free surface k_La in agitated systems is the product of the specific free surface area $a = \frac{A}{V_L}$ and the liquid-side oxygen mass transfer coefficient k_L. During the simulations, the dynamic free surface A is directly obtained from the used phase-field method, whereas the k_L is obtained from the mean free surface velocity. The simulations closely match the measured free surface k_La values over a wide range of operating conditions (Fig. 4D and E). Only at a stirrer speed of 540 rpm and 80 mL liquid volume, the simulations significantly underestimated the measured k_La (Fig. 4D). This was expected as this operating condition resulted in bubble entrainment due to vortex formation resulting in a sudden increase of the k_La. Excluding this outlier, the free surface k_La was predicted with a mean absolute error of 0.18 h^{-1} (relative error of 13.1%). This revalidates the approach from Thomas et al. [36] for predicting the free surface k_La. The increase of the free surface k_La with an increasing stirring speed can primarily be attributed to an increase in k_L, as the free surface remains mostly flat at lower stirring speeds (Supplementary data Figure S6).

3.1.3. Validation of particle suspension

We performed suspension experiments by imaging the bottom of the bioreactor filled with microcarrier-like particles and used the resulting size of the settled particle bed as validation data to assess our model's ability to predict particle suspension. The shapes and positions of the settled particle beds are qualitatively comparable between experiments and simulations (Fig. 4F).

In down-pumping mode, the simulations closely follow the experimental sizes of the settled particle bed for all investigated stirrer speeds (Fig. 4G left). However, for up-pumping stirrer speeds below 60 rpm, the predicted settled particle beds by the simulations are significantly smaller than observed experimentally (Fig. 4G right). Experimentally, the particles seemed to accumulate more easily into a single cluster resulting in a static settled particle bed, while during the simulations the particles moved more freely on the reactor's bottom. This difference can also be seen by the larger standard deviation of the settled particle bed size of the simulations compared to the experiments for both pumping modes (Fig. 4G). This could be a result of missing physical forces during the simulations. The used polyethylene particles are generally hydrophobic, and although a surfactant was used to suspend the particles in water, it might be that at very low liquid velocities these particle–particle hydrophobic interactions become significant. We note however that common microcarriers, like Cytodex-1, are generally hydrophilic and thus hydrophobic particle–particle forces would not be relevant. Furthermore, at higher particle packing fractions, lubrication forces become significant, the form of the drag coefficient changes, and accurate fluid–particle momentum coupling becomes more critical [62]. Given the generally lower liquid velocity near the bioreactor bottom in up-pumping mode, the aforementioned missing physical forces might explain the discrepancy between the experiments and our simulations.

Consequently, based on the settled particle bed size, the simulations would suggest up-pumping to result in better suspension than actually observed experimentally. However, when quantifying the number of particles on the reactor bottom, the simulations predict a better suspension for down-pumping compared to up-pumping (Fig. 4H). The observed model discrepancy in up-pumping mode might partially be caused the inability of the simulations to capture the cluster formation under these flow conditions, whereas the prediction of the number of unsuspended particles might be more reasonable.

We visually determined the N_{js} to be approximately 110 rpm for both up-pumping and down-pumping based on the 2 s criterion proposed by Zwietering [54]. This is roughly in agreement with the determined settled particle bed sizes using our image segmentation workflow, which approaches 0% at those stirring speeds (Fig. 4G). Note that the objective of quantifying the settled particle bed size through image segmentation served the purpose of validating the particle suspension behavior of our CFD–DEM simulations, not as an accurate method for determining the N_{js}.

The positioning of the sparger close to the reactor bottom resulted in a small fluid stagnation zone which kept a small number of particles on the reactor bottom for longer than 2 s at $N < 110$ rpm. However, at $N = 90$ rpm the number of particles on the reactor bottom was comparatively small. Moreover, the settled particle bed was not completely motionless and still resulted in a relatively frequent exchange (≈ 10 s) of particles between suspended and settled states. We therefore argue that a N_{js} of 90 rpm might be more appropriate to reduce the overall power input, although it relaxes the 2 s criterion from Zwietering [54]. Although visually up-pumping and down-pumping mode resulted in an equal N_{js}, at $N < N_{js}$ up-pumping resulted in a much larger settled particle bed (Fig. 4G), making down-pumping still the preferred operating mode as it generally achieves a better suspension at lower N.

Collignon et al. [28] made a similar observation where down-pumping resulted in a lower N_{js} than up-pumping, but with a much larger difference of 75 and 130 rpm, respectively. In contrast, Delbridge et al. [18] found a lower N_{js} for up-pumping than for down-pumping. Furthermore, we compared our N_{js} results with the empirical N_{js} correlation specifically for microcarriers from Loubière et al. [26] (Eq. S3), which predicted a N_{js} of 83 rpm for up-pumping and a N_{js} of 88 rpm for down-pumping. This deviates from our determined N_{js} of 110 rpm for both-pumping modes based on the strict 2 s criterion of Zwietering [54]. Overall, this highlights the sensitivity of the N_{js} to the reactor geometry (i.e., positioning of reactor internals and shape of reactor bottom), which is generally not included in such empirical correlations for N_{js} [26,54].

3.2. Case studies

Having thoroughly validated our model, and explored the impact of stirring speed on particle suspension, we now apply our model to characterize the 250 mL bioreactor under shear-sensitive stem cell microcarrier cultivation conditions. This means stirring at relatively low power input ($\frac{P}{V} < 5$ W/m^3), aeration only through the bioreactor headspace, and the presence of the commonly used Cytodex-1 microcarrier [12]. For each set of operating conditions, our model determined relevant scale-up parameters, including Po, P/V, t_{95}, and the free surface k_La. Simultaneously, microcarrier lifelines are used to assess the hydrodynamic stresses microcarriers are subject to during cultivations, as well as quantify the fraction of suspended microcarriers and assess microcarrier dispersion through the mean nearest neighbor distance $\bar{r}_{nn}$.

3.2.1. Effect of stirrer speed and pumping-mode

Up-pumping results in a higher predicted mean power number of 2.7 compared to down-pumping with a mean power number of 2.0 (Fig. 5B). This is likely caused by the orientation of the bioreactor internals and the dish-shaped reactor bottom (Fig. 1). In down-pumping

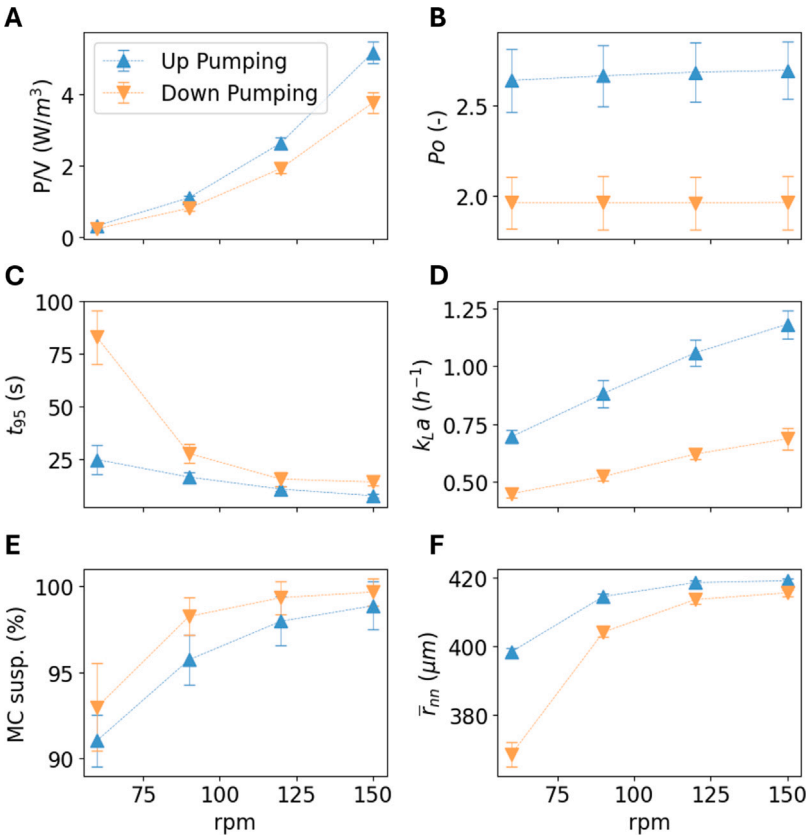


Fig. 5. Influence of stirrer speed for both up-pumping (▲) and down-pumping mode (▼) on Applikon MiniBio 250 mL hydrodynamics. (A) Volumetric power input P/V in W/m^3, (B) Impeller power number Po, (C) probe-based mixing time t_{95} in s, (D) free surface volumetric mass transfer coefficient k_La in h^{-1}, (E) percentage of suspended microcarriers according to the Lagrangian Zwietering [54] criterion, and (F) mean nearest neighbor particle distance r_{nn} in μm. These simulations were performed with a filling volume of 140 mL, stirrer height $C/H = 0.14$, and microcarrier concentration of 0.5 g/L.

mode, the impeller produces a mixed axial–radial flow which is then distributed via the dish bottom to the reactor walls resulting in lower resistance. In up-pumping mode, the fluid has to be pulled from the reactor bottom which is met with higher resistance due to the positioning of the bioreactor internals. This difference in pumping-mode is heavily geometry dependent as, for example, Delbridge et al. [18] found almost no difference in power number between up- and down-pumping mode in their system, whereas Zhu et al. [60] found a higher power number for down-pumping compared to up-pumping (2.2 and 1.8 respectively). The volumetric power input P/V was therefore higher for up-pumping than for down-pumping at the same stirrer speed.

This increase in power transfer in up-pumping mode also resulted in mixing times between 1.5 and 3 times lower than in down-pumping mode over the investigated stirring speeds (Fig. 5C), mainly due to better mixing near the reactor free surface. Similarly, the free surface k_La also increases up to 1.5 times when operating in up-pumping mode (Fig. 5D).

Conversely, the percentage of microcarriers in suspension is higher for down-pumping than for up-pumping, despite the fact that the volumetric power input is 35% higher for up-pumping (Fig. 5A and E). This is in agreement with our experimental observations that indicated a worse suspension when operating in up-pumping mode (Fig. 4). At 90 rpm specifically, which we consider a sufficiently suspended stirring speed N_{ss}, the percentage of microcarriers in suspension is 5 percentage points (%pt) higher for down-pumping than up-pumping. Yet, 90 rpm up-pumping resulted in a higher mean nearest neighbor particle distance $\bar{r}_{nn}$, which is a result of better particle dispersion in the top of the bioreactor, despite having a lower fraction of suspended microcarriers compared to down-pumping.

A typical rule-of-thumb for animal cell culture to determine whether turbulent eddies are damaging originates from Croughan et al. [63], who found a significant decrease in cell viability when the mean Kolmogorov length scale $\overline{\lambda_k}$ fell below two-thirds of the microcarrier size. Fig. 6A shows that at 90 rpm the $\overline{\lambda_k}$ for both pumping modes stay above two-thirds of the median microcarrier size (170 μm), indicating that these hydrodynamic conditions are generally favorable. Furthermore, the λ_k distribution shows that for down-pumping 20.4% of hydrodynamic conditions encountered by the microcarriers contain eddies smaller than two-thirds the median microcarrier size, while for up-pumping this becomes 26.5%. The observations based on λ_k are in agreement with the Accumulated Hydrodynamic Damage metric, which shows a steeper increase over time for up-pumping compared to down-pumping (Fig. 6B).

This demonstrates that at 90 rpm down-pumping results in less overall hydrodynamic damage than up-pumping, while simultaneously a higher percentage of suspended microcarriers is achieved. Although similar small-scale bioreactors exist (e.g., Ambr®250 from Sartorius, DASbox® Mini Bioreactor from Eppendorf), the effect of the pumping mode cannot necessarily be transferred between different systems due to geometrical differences. Therefore, deciding on the optimal pumping mode requires system specific studies, as well as determining which bioreactor performance metrics are most critical. In the case of minimal hydrodynamic stress to achieve microcarrier suspension, we consider down-pumping the preferred pumping mode in the Applikon MiniBio 250 mL.

3.2.2. *Effect of impeller height*

Increasing the impeller height from $\frac{C}{H} = 0.14$ to $\frac{C}{H} = 0.22$ reduces the number of microcarriers in suspension by 5%pts, while the free surface k_La increases from 0.45 h^{-1} to 0.51 h^{-1} (Fig. 7). The mixing time t_{95} dramatically decreases from 44.6 to 21.1 s, but this difference

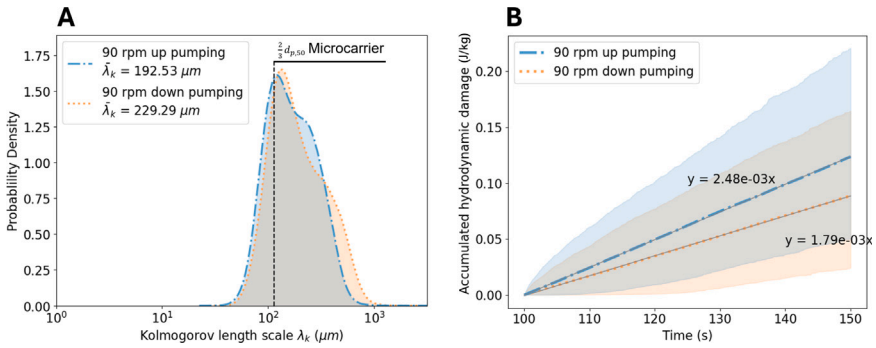


Fig. 6. Influence of pumping mode on hydrodynamic stresses at sufficient-suspension stirrer speed of 90 rpm. (A) Kolmogorov length scale (λ_k) distributions for up-pumping (dash-dot line) and down-pumping (dotted line) mode. The mean Kolmogorov length scale ($\overline{\lambda_k}$) is included in the legend. Vertical dashed line represents two-thirds of the median Cytodex-1 microcarrier size, a typically used rule-of-thumb from Croughan et al. [63] to define whether turbulent eddies are potentially damaging to cells on microcarriers. (B) Accumulated Hydrodynamic Damage (ADH) of microcarrier lifelines for up-pumping (dash-dot line) and down-pumping (dotted line) mode. The lines represent the mean ADH and the shaded area the 95% percentile interval. Both the λ_k-distribution and ADH plot are constructed directly from the microcarrier lifelines.

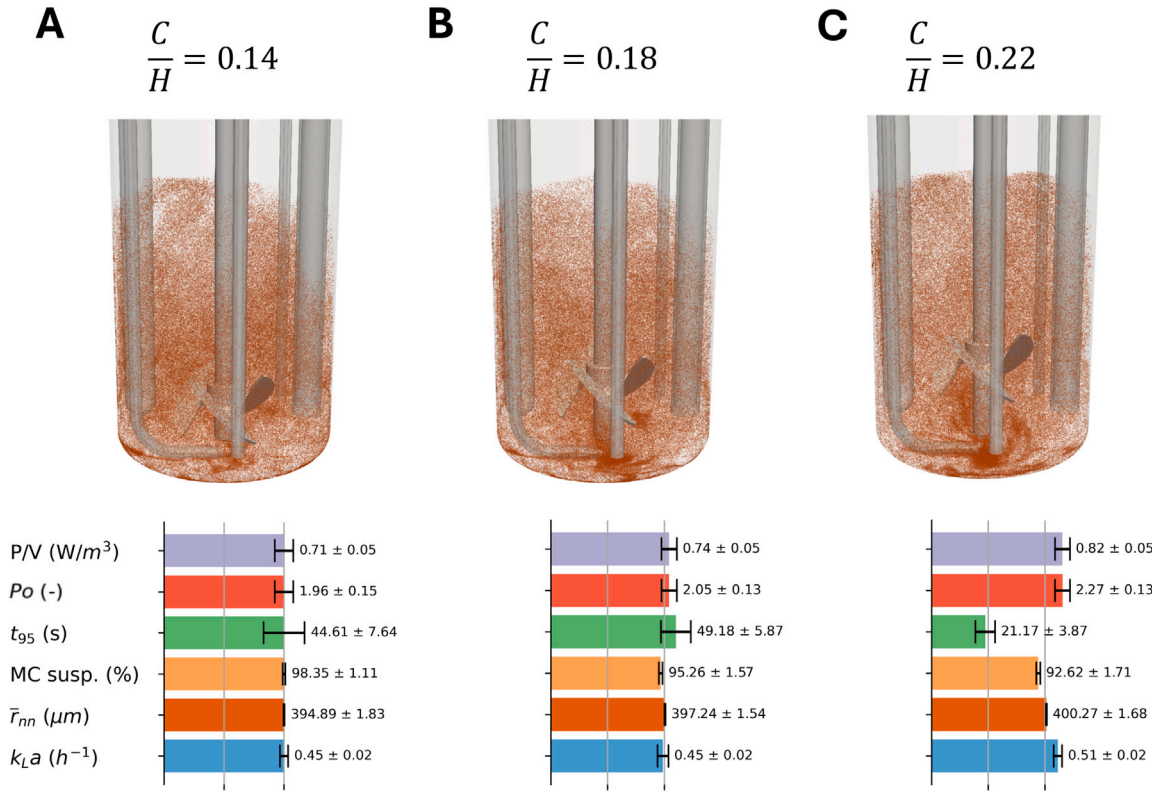


Fig. 7. Influence of stirrer height on bioreactor performance parameters at $C/H = 0.14$ (A), $C/H = 0.18$ (B) and $C/H = 0.22$ (C). Instantaneous snapshots of microcarrier (orange particles) suspension are shown. Horizontal bar plots represent mean values of bioreactor performance parameters including volumetric power input P/V, impeller power number Po, probe-based mixing time t_{95}, percentage of suspended microcarriers, and mean nearest neighbor distance $\bar{r}_{nn}$. The error bars originate from the inherent transient nature of the LB-LES method and represent the $\pm 1SD$ confidence interval over the recorded flow time, with the exception for t_{95} which represents the $\pm 1SD$ of six distinct numerical tracers with varying injection times. These simulations were performed with a filling volume of 160 mL, 90 rpm down-pumping impeller, and microcarrier concentration of 0.5 g/L.

is just an indicator of poor mixing near the reactor free surface, which worsens when lowering the impeller height. Nonetheless, these mixing times are still order of magnitude smaller than $\frac{1}{k_La}$ and human (stem) cell oxygen uptake kinetics [6], and the bioreactor can therefore still be considered ideally mixed. The power number also increases from 1.96 to 2.27, likely due to less efficient fluid dispersion via the reactor bottom and more flow resistance from the bioreactor internals.

In terms of hydrodynamic stress, the effect of the impeller height is not strong since roughly the same P/V and microcarrier circulation patterns are maintained (Fig. 8). The $\overline{\lambda_k}$ decreases from 244 μm to 211 μm when increasing the impeller height, caused by the slight increase in P/V. Yet, the minimum Kolmogorov length scale $\lambda_{k,min}$ (corresponding to highest local energy dissipation rate) remains relatively constant with 25.5 μm at $\frac{C}{H} = 0.14$, to 26.5 μm at $\frac{C}{H} = 0.18$, and to 25.3 μm at $\frac{C}{H} = 0.22$. In contrast, the hydrodynamic conditions where the turbulent eddies are smaller than two-thirds of the median microcarrier size increases from 16.1% at $\frac{C}{H} = 0.22$, to 18.0% at $\frac{C}{H} = 0.18$, to 19.4% at $\frac{C}{H} = 0.14$, indicating that microcarriers experience more damaging eddies at lower impeller height (Fig. 8A). This is in agreement with the observed increase in Accumulated Hydrodynamic Damage, where

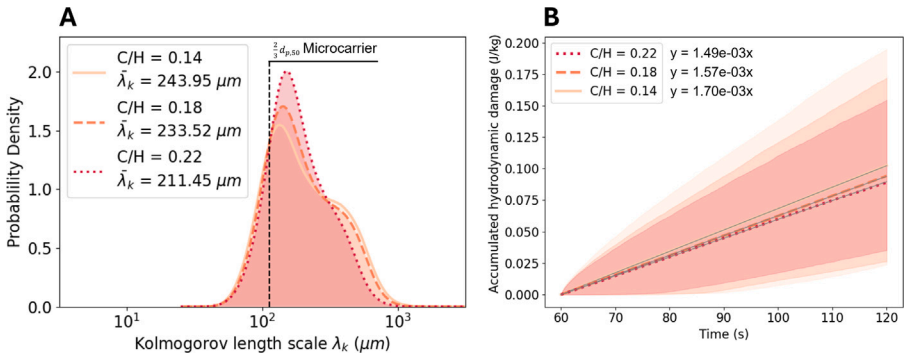


Fig. 8. Influence of stirrer height on hydrodynamic stress at $C/H = 0.14$ (solid line), $C/H = 0.18$ (dashed line) and $C/H = 0.22$ (dotted line). (A) Kolmogorov length scale (λ_k) distributions for up-pumping (dash-dot line) and down-pumping (dotted line) mode. The mean Kolmogorov length scale ($\overline{\lambda_k}$) is included in the legend. Vertical dashed line represents two-thirds of the median Cytodex-1 microcarrier size, a typically used rule-of-thumb from Croughan et al. [63] to define whether turbulent eddies are potentially damaging to cells on microcarriers. (B) Accumulated Hydrodynamic Damage (ADH) of microcarrier lifelines. The lines represent the mean ADH and the shaded area the 95% percentile interval. Both the λ_k-distribution and ADH plot are constructed directly from the microcarrier lifelines.

a lower impeller height results to a slight increase in hydrodynamic stress (Fig. 8B). This apparent increase in hydrodynamic stress when lowering the impeller height is simply because more microcarriers are in suspension.

3.2.3. *Effect of liquid filling volume*

The bioreactor filling volume is another operating parameter which, in lab-scale, is usually dictated by the cellular nutrient requirements (in batch-mode) or required oxygen transfer rate. Increasing the filling volume results in more nutrient availability but generally reduces the k_La. In addition, microcarrier suspension and dispersion through the entire vessel might be harder to achieve at higher filling volumes.

Fig. 9 shows that at $V_L = 200$ mL the t_{95} was still not reached after 240 s of flow time, clearly demonstrating poor mixing behavior in the top of the reactor compared to a t_{95} of 36 s at $V_L = 140$ mL, and a t_{95} of 8 s at $V_L = 80$ mL. This is also reflected in the microcarrier dispersion, where at $V_L = 200$ mL the microcarriers fail to reach the top part of the reactor, which is also reflected in a lower $\bar{r}_{nn}$ of 369 μm. At $V_L = 140$ mL, a decent dispersion of microcarries in the full working volume is achieved with a $\bar{r}_{nn}$ of 405 μm, but is slightly sub-optimal when compared to $V_L = 80$ mL where $\bar{r}_{nn}$ is 412 μm.

As a consequence of poor mixing in the top of the reactor, our simulations predict a low free surface k_La of 0.34 h^{-1} at $V_L = 200$ mL, compared to 0.55 h^{-1} at $V_L = 140$ mL, and 1.40 h^{-1} at $V_L = 80$ mL. Compared to $V_L = 80$ mL, increasing the working volume to 200 mL results in a decrease of the oxygen transfer rate (OTR) by a factor $\frac{1.40}{0.34} \approx 4.1$. This is significantly more than the expected decrease of a factor $\frac{200}{80} = 2.5$ of the specific interfacial area, highlighting the dependence of k_L on the distance of the free surface to the impeller. Whether a sufficiently high OTR can be achieved through the free surface entirely depends on the cell specific oxygen consumption rate and the desired cell density. Nevertheless, with our model predictions we improve the understanding of the hydrodynamic culture conditions and support scale-up of such stem cell microcarrier processes to larger scale.

In terms of hydrodynamic stress, lowering the liquid volume results in a higher Accumulated Hydrodynamic Damage as the circulation time around the impeller becomes shorter (Fig. 10B). Furthermore, due to better microcarrier dispersion at $V_L = 80$ mL the λ_k-distribution becomes more homogeneous (Fig. 10A) and the bimodal nature of the distribution disappears. At $V_L = 140$ and $V_L = 200$, this bimodal λ_k distribution shape is likely a consequence of a slower circulation loop in the top of the reactor. A more uniform λ_k-distribution at $V_L = 80$ mL might be advantageous when the objective is to create homogeneous cell aggregates. Increasing the filling volume from $V_L = 140$ mL to $V_L = 200$ mL does not change the hydrodynamic stress significantly because the microcarriers are not getting dispersed into the additional added fluid.

This highlights the advantage of using the microcarrier perspective to quantify the hydrodynamic stresses, as taking the λ_k distribution from the fluid directly would have resulted in a significant increase in $\overline{\lambda_k}$ when increasing V_L. Furthermore, scaling up using a constant P/V could become misleading as this usually assumes a constant mean energy dissipation rate $\bar{\varepsilon}$ experienced by the cells, which is not necessarily true when the microcarriers are not fully dispersed.

Overall, our results suggest that with a single down-pumping elephant ear impeller at $\frac{C}{H} = 0.14$ and at 90 rpm, the maximum operable working volume is around 140 mL. Increasing V_L further results in poor mixing, poor microcarrier dispersion, and a low free surface k_La. If operation at higher working volumes is desired, we recommend a dual impeller configuration, as described in Supplementary data Section S11. The investigation of the dual impeller configuration showed that the inter-impeller ($\frac{S}{D}$) distance has a great effect on the power transfer, and thus also on the hydrodynamic stress. In this setup at $V_L = 200$ mL, a $\frac{S}{D} = 1.5$ resulted in two hydrodynamically independent operating impellers, yielding the best bioreactor performance in terms of mixing time, free surface k_La and microcarrier dispersion, while maintaining similar levels of hydrodynamic stress as a single impeller configuration at $V_L = 80$ mL (Fig. 10A and B).

4. Concluding remarks

In this work, we developed a CFD–DEM model of the fluid flow and microcarriers inside a 250 mL stirred-tank bioreactor, which (i) accurately determined common scale-up parameters such as volumetric power input (P/V), mixing time (t_{95}), and free surface volumetric oxygen mass transfer coefficient (k_La); and (ii) modeled microcarriers as Lagrangian particles which enabled quantification of suspension and hydrodynamic stresses directly from microcarrier lifelines. We emphasized the importance of using the Lagrangian lifeline perspective as microcarriers might not be fully suspended and dispersed under typical stem cell operating conditions ($P/V \approx 1$ W/m^3) and therefore do not experience the fluid hydrodynamics equally throughout the bioreactor. The physical validity of our CFD–DEM model was evaluated through various experiments, which demonstrated that the model could quantify the P/V, t_{95}, and k_La within 20% of the experimental values.

Although generally good agreement was found between the particle suspension experiments and our model's predictions, the physical accuracy of our model could be improved. For one, simplifications were made in the included fluid–particle forces to keep computational times tractable, by neglecting for example lift forces and the Basset History force as done previously [43,51], even though these forces might not

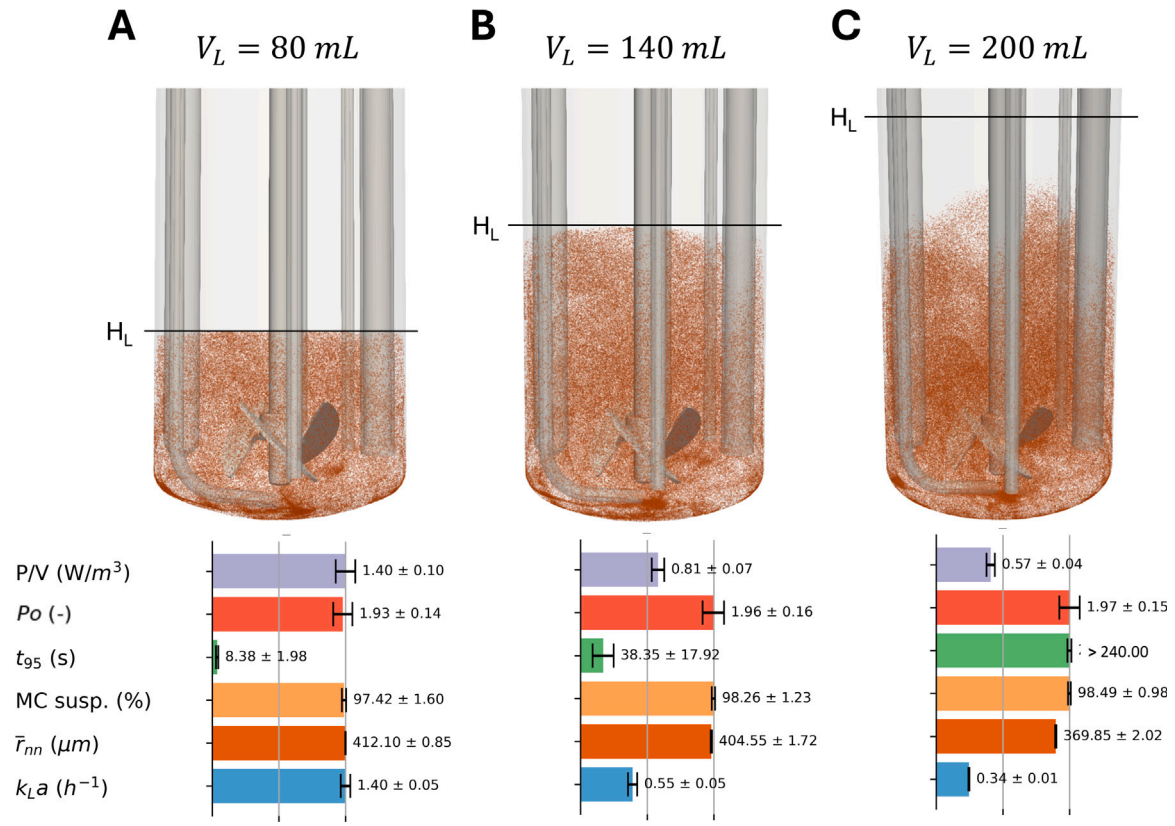


Fig. 9. Influence of filling volume on bioreactor performance parameters at $V_L = 80$ (A), $V_L = 140$ (B) and $V_L = 200$ (C). Instantaneous snapshots of microcarrier (orange particles) suspension are shown with H_L representing the liquid height of bioreactor. Horizontal bar plots represent mean values of bioreactor performance parameters including volumetric power input P/V, impeller power number Po, probe-based mixing time t_{95}, percentage of suspended microcarriers, and mean nearest neighbor distance $\bar{r}_{nn}$. The error bars originate from the inherent transient nature of the LB-LES method and represent the $\pm 1SD$ confidence interval over the recorded flow time, with the exception for t_{95} which represents the $\pm 1SD$ of six distinct numerical tracers with varying injection times. These simulations were performed at 90 rpm with a down-pumping impeller at $C/H = 0.14$, and microcarrier concentration of 0.5 g/L.

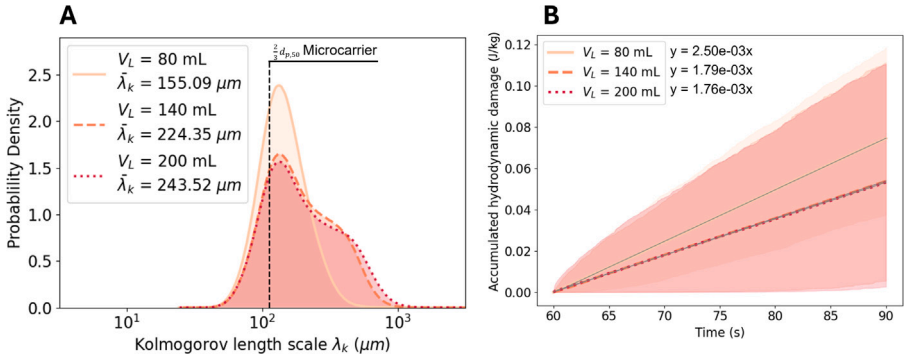


Fig. 10. Influence of filling volume on hydrodynamic stress at $V_L = 80$ mL (solid line), $V_L = 140$ mL (dashed line) and $V_L = 200$ mL (dotted line). (A) Kolmogorov length scale (λ_k) distributions for up-pumping (dash-dot line) and down-pumping (dotted line) mode. The mean Kolmogorov length scale ($\overline{\lambda_k}$) is included in the legend. Vertical dashed line represents two-thirds of the median Cytodex-1 microcarrier size, a typically used rule-of-thumb from Croughan et al. [63] to define whether turbulent eddies are potentially damaging to cells on microcarriers. (B) Accumulated Hydrodynamic Damage (ADH) of microcarrier lifelines. The lines represent the mean ADH and the shaded area the 95% percentile interval. Both the λ_k-distribution and ADH plot are constructed directly from the microcarrier lifelines.

be negligible [62]. Furthermore, a simplified particle–fluid coupling based only on the gravity-buoyancy force was used, since the more physically accurate third-law coupling resulted in numerically unstable simulations. This is a common problem in numerical particle–fluid coupling due to emerging discontinuities for which various smoothing routines of the momentum exchange field have been suggested [51, 56]. Experimental techniques such as 4D particle tracking velocimetry would be suitable to collect quantitative validation data on particle velocities and accelerations to further understand how the aforementioned simplifications affect the simulated particle trajectories [64]. In addition, Hertzian soft-sphere contact model parameters were chosen semi-empirically based on images from the suspension experiments. Although this approach of using experimental data to calibrate the DEM parameters is common practice [65,66], more advanced parameter fitting routines based on multi objective optimization could be used on

our suspension image dataset to obtain more accurate DEM parameters [67].

The simulations showed that a down-pumping elephant ear impeller resulted in a better suspension at a lower P/V than when operating in up-pumping mode. For shear-sensitive stem cell microcarrier cultures, we found a generally good suspension when operated with a volumetric power input in the range of $0.5-3$ W/m^3. This resulted in mixing times in the order of $10-50$ seconds and free surface k_La in the order of $0.5-2$ h^{-1}. Typically for stem cell cultures, the oxygen transfer rate is not limiting at these lab-scales. However, when scaling up the process to larger bioreactors (i.e., 200–2000 L) the k_La likely becomes limiting, which is why we argue for quantifying the k_La early-on during process development. When combined with measurements of stem cell specific oxygen uptake rates, projections can be made at which scale free surface k_La becomes limiting and appropriate scale-down experiments can be designed to study, for example, the impact of gas sparging on cell viability and differentiation potential.

We used the microcarrier lifelines to study hydrodynamic stress via the Kolmogorov length scale distribution, and through the Accumulated Hydrodynamic Damage by integrating energy dissipation rate time series. In future work, this lifeline analysis can be extended to quantify the frequency and time exposure of cells or microcarriers to certain ϵ thresholds. It has namely be suggested that hydrodynamic damage results from a combination of stress magnitude and exposure duration [68,69], which can naturally be quantified via the microcarrier lifelines. This becomes especially meaningful when combined with experimental stem cell bioreactor results, such as cell viability or differentiation potential, as this would allow for correlating specific ϵ thresholds to cellular responses. Furthermore, particle residence time distributions on the reactor bottom and particle–particle collision frequencies can be quantified with DEM, from which mechanistic insights can be obtained on other relevant processes, such as cell-microcarrier attachment or stem cell aggregation.

To conclude, we encourage the use of our detailed Applikon MiniBio 250 mL characterization results in combination with experimental stem cell cultivation work, to better understand the link between hydrodynamic conditions and the performance of the stem cell bioreactor cultivation. Although throughout this work we primarily focused on suspension and hydrodynamic stress of microcarriers, we believe that our results and modeling approach can be translated relatively easily to the cultivation of stem cell aggregates such as EBs upon determination of their size and density. Moreover, we expect our model to be scale-independent as our approach is grounded in first-principles physics, enabling application to larger bioreactors or even different cultivation systems. Applying such detailed CFD–DEM models to both lab-scale and industrial-scale bioreactors will decrease scale-up risk due to hydrodynamic changes and reduce experimental efforts to identify optimal operating conditions, which will ultimately accelerate scale-up of shear-sensitive stem cell microcarrier culture production processes.

Nomenclature

Abbreviations

CFD	Computational Fluid Dynamics
DEM	Discrete Element Method
DO	Relative dissolved oxygen concentration
E-E	Eulerian–Eulerian
E-L	Eulerian–Lagrangian
EB	Embryoid Body
hiPSC	Human Inducible Pluripotent Stem Cell
LB	Lattice Boltzmann
LES	Large Eddy Simulation
MC	Microcarrier
MSC	Mesenchymcal Stem Cell
SD	Standard Deviation

Greek

α_s	Particle volume fraction (–)
Δt_{DEM}	DEM timestep (s)
Δt_f	Fluid timestep (s)
Δx	Grid spacing (m)
$\delta_{n,ij}$	Normal particle overlap (m)
$\delta_{t,ij}$	Tangential particle overlap (m)
$\dot{\delta}_{n,ij}$	Time derivative of normal particle overlap (m s^{-1})
$\dot{\delta}_{t,ij}$	Time derivative of tangential particle overlap (m s^{-1})
ϵ	Energy dissipation rate (W kg^{-1})
ϵ_p	Restitution coefficient (–)
$\gamma_{n,ij}$	Normal damping coefficient (N s m^{-1})
$\gamma_{t,ij}$	Tangential damping coefficient (N s m^{-1})
λ_k	Kolmogorov length scale (m)
μ	Fluid dynamic viscosity (Pa s^{-1})
μ_p	Sliding friction coefficient (–)
ν	Fluid kinematic viscosity (m$^{2\ s^{-1}}$)
ν_p	Poisson's ratio (–)
ν_t	Turbulent viscosity (m$^{2\ s^{-1}}$)
ω	Angular velocity (rad s^{-1})
Ω_i	Collision operator (kg m^{-3})
ϕ	Phase-field order parameter (–)
ρ_f	Fluid density (kg m^{-3})
ρ_g	Gas density (kg m^{-3})
ρ_p	Particle density (kg m^{-3})
σ	Surface tension (N m^{-1})
τ	Torque (N m)
τ_{xy}	Fluid shear stress (Pa)

Latin

$\mathbf{f}_{ij}$	Particle–particle contact force (N)
$\mathbf{f}_{n,ij}$	Normal particle–particle contact force (N)
$\mathbf{f}_{t,ij}$	Tangential particle–particle contact force (N)
A	Area (m$^{2)}$
a	Specific interfacial area (m^{-1})
C	Off-bottom clearance (m)
c	Scalar concentration (–)
$c^*_{O_2,L}$	Oxygen saturation concentration (mol L^{-1})
C_D	Drag coefficient (–)
c_i	Discrete lattice velocity (m s^{-1})
C_s	Smagorinsky coefficient (–)
$c_{O_2,L}$	Dissolved oxygen concentration (mol L^{-1})
D	Impeller diameter (m)
D_m	Molecular diffusion coefficient (m$^{2\ s^{-1}}$)
d_p	Particle diameter (m)
F_i^b	Buoyancy force on particle i (N)
F_i^d	Drag force on particle i (N)
F_i^g	Gravity force acting on particle i (N)
$F_i^{f\rightarrow p}$	Fluid forces acting on particle i (N)
$F^{p\rightarrow f}$	Particle forces acting on fluid (N)
$F_i^{p\rightarrow p}$	Particle–particle interaction forces on particle i (N)
F_i^{vm}	Virtual mass force on particle i (N)
f_i	Discrete-velocity distribution function (kg m^{-3})
f_s	Surface tension force density (N m^{-3})
f_{ext}	External force densities (N m^{-3})
g	Gravitational constant (m s^{-2})
G^*_{ij}	Equivalent shear modulus (Pa)
H	Tank height (m)

H_L	Liquid height (m)
k_La	Volumetric mass transfer coefficient (s^{-1})
k_L	Liquid-side mass transfer coefficient (m s^{-1})
$k_{n,ij}$	Normal stiffness coefficient (N m^{-1})
$k_{t,ij}$	Tangential stiffness coefficient (N m^{-1})
M	Mobility parameter ($m^{2\ s^{-1}}$)
m^*_{ij}	Equivalent mass (kg)
m_i	Particle mass (kg)
N	Impeller rotational speed (s^{-1})
n	Interface normal vector (–)
N_p	Number of particles (–)
N_{js}	Just-suspension stirring speed (s^{-1})
N_{ss}	Sufficient-suspension stirring speed (s^{-1})
P	Impeller power input (W)
p	Fluid pressure (Pa)
Po	Impeller power number (–)
R^*_{ij}	Equivalent radius (m)
r_{nn}	Particle nearest neighbor distance (m)
Re_{imp}	Impeller Reynolds number (–)
Re_p	Particle Reynolds number (–)
S	Inter-impeller distance (m)
T	Tank diameter (m)
t_{95}	Mixing time (s)
$t_{probe,90}$	Probe response time (s)
u	Fluid velocity (m s^{-1})
V_f	Free surface velocity (m s^{-1})
v_i	Particle velocity (m s^{-1})
V_L	Filling volume (m^{-3})
V_p	Particle volume (m^3)
W	Interface width (m)
Y	Young's modulus (Pa)
Y^*_{ij}	Equivalent Young's modulus (Pa)
AHD	Accumulated Hydrodynamic Damage (J kg^{-1})
$\|\|S\|\|$	Norm of the resolved strain rate tensor (s^{-1})

CRediT authorship contribution statement

Ramon D. van Valderen: Writing – review & editing, Writing – original draft, Visualization, Validation, Methodology, Investigation, Formal analysis, Data curation, Conceptualization. **Brenda E. Juarez-Garza:** Writing – review & editing, Investigation. **Stijn de Smit:** Writing – review & editing, Investigation. **Marcel Ottens:** Writing – review & editing, Supervision, Funding acquisition. **Cees Haringa:** Writing – review & editing, Supervision, Funding acquisition, Conceptualization.

Declaration of generative AI use

During the preparation of this work the authors used ChatGPT model GPT-4o in order to implement the Python codes for the pH probe signal deconvolution and particle suspension image segmentation workflow. After using this tool, the authors reviewed and edited the code as needed including documentation and take full responsibility for the content of the published article.

Declaration of competing interest

The authors declare that they have no known competing financial interests or personal relationships that could have appeared to influence the work reported in this paper.

Acknowledgments

This work was performed within the TRACER consortium, which is funded by the ZonMw PSIDER programme (grant number 10250022110001). The staff of M-STAR CFD, in particular Johannes Wutz, was thanked for their support, as well as Rowin Timmermans from SecureCell for helping us setup automated k_La measurements. We thank Tom van Arragon from Getinge for his support with the Applikon MiniBio 250 mL. The authors are grateful to colleagues from the TRACER consortium and the department of Biotechnology from TU Delft for their valuable insights and productive discussions.

Appendix A. Supplementary data

Supplementary material related to this article can be found online at https://doi.org/10.1016/j.bej.2026.110365.

Data availability

The experimental data, code for the pH probe lag time correction method, and code for the image segmentation workflow are openly available on 4TU.ResearchData at 10.4121/2a82e089-a272-47be-8043-d505dba03339. The simulation data of this study is available from the corresponding author upon reasonable request.

References

[1] P.E. Mulaudzi, H. Abrahamse, A. Crous, Insights on three dimensional organoid studies for stem cell therapy in regenerative medicine, Stem Cell Rev. Rep. 20 (2) (2024) 509–523, http://dx.doi.org/10.1007/s12015-023-10655-6.

[2] K. Thanaskody, A.S. Jusop, G.J. Tye, W.S. Wan Kamarul Zaman, S.A. Dass, F. Nordin, MSCs vs. iPSCs: potential in therapeutic applications, Front. Cell Dev. Biol. 10 (2022) 1005926, http://dx.doi.org/10.3389/fcell.2022.1005926.

[3] C. Brown, C. McKee, S. Bakshi, K. Walker, E. Hakman, S. Halassy, D. Svinarich, R. Dodds, C.K. Govind, G.R. Chaudhry, Mesenchymal stem cells: cell therapy and regeneration potential, J. Tissue Eng. Regen. Med. 13 (9) (2019) 1738–1755, http://dx.doi.org/10.1002/term.2914.

[4] R.M. Aly, Current state of stem cell-based therapies: An overview, Stem Cell Investig. 7 (2020) 8, http://dx.doi.org/10.21037/sci-2020-001.

[5] S. Demirci, A. Leonard, J.F. Tisdale, Hematopoietic stem cells from pluripotent stem cells: clinical potential, challenges, and future perspectives, Stem Cells Transl. Med. 9 (12) (2020) 1549–1557, http://dx.doi.org/10.1002/sctm.20-0247.

[6] S. Jung, K.M. Panchalingam, R.D. Wuerth, L. Rosenberg, L.A. Behie, Large-scale production of human mesenchymal stem cells for clinical applications, Biotechnol. Appl. Biochem. 59 (2) (2012) 106–120, http://dx.doi.org/10.1002/bab.1006.

[7] A.M. de Soure, A. Fernandes-Platzgummer, C.L. da Silva, J.M.S. Cabral, Scalable microcarrier-based manufacturing of mesenchymal stem/stromal cells, J. Biotech. 236 (2016) 88–109, http://dx.doi.org/10.1016/j.jbiotec.2016.08.007.

[8] M. Stephenson, W. Grayson, Recent advances in bioreactors for cell-based therapies, F1000Research 7 (2018) http://dx.doi.org/10.12688/f1000research.12533.1, F1000 Faculty Rev–517.

[9] Q.A. Rafiq, K.M. Brosnan, K. Coopman, A.W. Nienow, C.J. Hewitt, Culture of human mesenchymal stem cells on microcarriers in a 5 l stirred-tank bioreactor, Biotechnol. Lett. 35 (8) (2013) 1233–1245, http://dx.doi.org/10.1007/s10529-013-1211-9.

[10] M.A. Teale, S.L. Schneider, D. Eibl, R. Eibl, Process intensification in human pluripotent stem cell expansion with microcarriers, Processes 12 (3) (2024) 426, http://dx.doi.org/10.3390/pr12030426.

[11] J. Sivalingam, A.T.-L. Lam, H.Y. Chen, B.X. Yang, A.K.-L. Chen, S. Reuveny, Y.-H. Loh, S.K.-W. Oh, Superior red blood cell generation from human pluripotent stem cells through a novel microcarrier-based embryoid body platform, Tissue Eng. Part C, Methods 22 (8) (2016) 765–780, http://dx.doi.org/10.1089/ten.TEC.2015.0579.

[12] E. Varga, E. Brandsma, B.E. Juarez-Garza, R.P.E. Ramlal, J.J. Karrich, A. Laurent, A. Chavli, R. Paskel, K. Fu, R.A. Flavell, M. von Lindern, D. Amsen, M.E. Klijn, E. van den Akker, Large-scale production of transfusion-ready red blood cells from induced pluripotent stem cells, Adv. Sci. 12 (38) (2025) e04725, http://dx.doi.org/10.1002/advs.202504725.

[13] G. Pettinato, X. Wen, N. Zhang, Engineering strategies for the formation of embryoid bodies from human pluripotent stem cells, Stem Cells Dev. 24 (14) (2015) 1595–1609, http://dx.doi.org/10.1089/scd.2014.0427.

[14] C.Y. Sargent, G.Y. Berguig, M.A. Kinney, L.A. Hiatt, R.L. Carpenedo, R.E. Berson, T.C. McDevitt, Hydrodynamic modulation of embryonic stem cell differentiation by rotary orbital suspension culture, Biotechnol. Bioeng. 105 (3) (2010) 611–626, http://dx.doi.org/10.1002/bit.22578.

[15] A. Sen, M.S. Kallos, L.A. Behie, Effects of hydrodynamics on cultures of mammalian neural stem cell aggregates in suspension bioreactors, Ind. Eng. Chem. Res. 40 (23) (2001) 5350–5357, http://dx.doi.org/10.1021/ie001107y.

[16] A.P. Van Winkle, I.D. Gates, M.S. Kallos, Mass transfer limitations in embryoid bodies during human embryonic stem cell differentiation, Cells Tissues Organs 196 (1) (2012) 34–47, http://dx.doi.org/10.1159/000330691.

[17] H.Y. Farsani, J. Wutz, B. DeVincentis, J.A. Thomas, S.P. Motevalian, Modeling mass transfer in stirred microbioreactors, Chem. Eng. Sci. 248 (2022) 117146, http://dx.doi.org/10.1016/j.ces.2021.117146.

[18] J.N. Delbridge, T.A. Barrett, A. Ducci, M. Micheletti, Power, mixing and flow dynamics of the novel Allegro™stirred tank reactor, Chem. Eng. Sci. 271 (2023) 118545, http://dx.doi.org/10.1016/j.ces.2023.118545.

[19] M. Kuschel, J. Wutz, M. Salli, D. Monteil, T. Wucherpfennig, CFD supported scale up of perfusion bioreactors in biopharma, Front. Chem. Eng. 5 (2023).

[20] B.S. Borys, E.L. Roberts, A. Le, M.S. Kallos, Scale-up of embryonic stem cell aggregate stirred suspension bioreactor culture enabled by computational fluid dynamics modeling, Biochem. Eng. J. 133 (2018) 157–167, http://dx.doi.org/10.1016/j.bej.2018.02.005.

[21] T. Dang, B.S. Borys, S. Kanwar, J. Colter, H. Worden, A. Blatchford, M.S. Croughan, T. Hossan, D.E. Rancourt, B. Lee, M.S. Kallos, S. Jung, Computational fluid dynamic characterization of vertical-wheel bioreactors used for effective scale-up of human induced pluripotent stem cell aggregate culture, Can. J. Chem. Eng. 99 (11) (2021) 2536–2553, http://dx.doi.org/10.1002/cjce.24253.

[22] J. Zhang, Y. Peng, M. Guo, C. Li, Large-scale expansion of human umbilical cord-derived mesenchymal stem cells in a stirred suspension bioreactor enabled by computational fluid dynamics modeling, Bioengineering 9 (7) (2022) 274, http://dx.doi.org/10.3390/bioengineering9070274.

[23] R.D. van Valderen, B.E. Juarez-Garza, M.E. Klijn, M. Ottens, C. Haringa, Implicit large eddy simulations for hydrodynamic stress characterization in 125 mL shake flasks for stem cell cultures, Biochem. Eng. J. 219 (2025) 109734, http://dx.doi.org/10.1016/j.bej.2025.109734.

[24] S. Kaiser, V. Jossen, C. Schirmaier, D. Eibl, S. Brill, C. van den Bos, R. Eibl, Fluid flow and cell proliferation of mesenchymal adipose-derived stem cells in small-scale, stirred, single-use bioreactors, Chem. Ing. Tech. 85 (1–2) (2013) 95–102, http://dx.doi.org/10.1002/cite.201200180.

[25] A. Delafosse, C. Loubière, S. Calvo, D. Toye, E. Olmos, Solid-liquid suspension of microcarriers in stirred tank bioreactor – experimental and numerical analysis, Chem. Eng. Sci. 180 (2018) 52–63, http://dx.doi.org/10.1016/j.ces.2018.01.001.

[26] C. Loubière, A. Delafosse, E. Guedon, I. Chevalot, D. Toye, E. Olmos, Dimensional analysis and CFD simulations of microcarrier 'just-suspended' state in mesenchymal stromal cells bioreactors, Chem. Eng. Sci. 203 (2019) 464–474, http://dx.doi.org/10.1016/j.ces.2019.04.001.

[27] C. Haringa, An analysis of organism lifelines in an industrial bioreactor using lattice-Boltzmann CFD, Eng. Life Sci. n/a (n/a) (2022) http://dx.doi.org/10.1002/elsc.202100159.

[28] M.-L. Collignon, A. Delafosse, S. Calvo, C. Martin, A. Marc, D. Toye, E. Olmos, Large-eddy simulations of microcarrier exposure to potentially damaging eddies inside mini-bioreactors, Biochem. Eng. J. 108 (2016) 30–43, http://dx.doi.org/10.1016/j.bej.2015.10.020.

[29] J.D. Berry, P. Liovic, I.D. Šutalo, R.L. Stewart, V. Glattauer, L. Meagher, Characterisation of stresses on microcarriers in a stirred bioreactor, Appl. Math. Model. 40 (15) (2016) 6787–6804, http://dx.doi.org/10.1016/j.apm.2016.02.025.

[30] M. Rotondi, N. Grace, J. Betts, N. Bargh, E. Costariol, B. Zoro, C.J. Hewitt, A.W. Nienow, Q.A. Rafiq, Design and development of a new Ambr250® bioreactor vessel for improved cell and gene therapy applications, Biotechnol. Lett. 43 (5) (2021) 1103–1116, http://dx.doi.org/10.1007/s10529-021-03076-3.

[31] M.A. Garcia-Briones, R.S. Brodkey, J.J. Chalmers, Computer simulations of the rupture of a gas bubble at a gas—Liquid interface and its implications in animal cell damage, Chem. Eng. Sci. 49 (14) (1994) 2301–2320, http://dx.doi.org/10.1016/0009-2509(94)E0038-R.

[32] J. Wu, Mechanisms of animal cell damage associated with gas bubbles and cell protection by medium additives, J. Biotech. 43 (2) (1995) 81–94, http://dx.doi.org/10.1016/0168-1656(95)00133-7.

[33] A.W. Nienow, Reactor engineering in large scale animal cell culture, Cytotechnology 50 (1) (2006) 9, http://dx.doi.org/10.1007/s10616-006-9005-8.

[34] G.M. Pigeau, E. Csaszar, A. Dulgar-Tulloch, Commercial scale manufacturing of allogeneic cell therapy, Front. Med. 5 (2018) http://dx.doi.org/10.3389/fmed.2018.00233.

[35] B. Lee, S. Jung, Y. Hashimura, M. Lee, B.S. Borys, T. Dang, M.S. Kallos, C.A.V. Rodrigues, T.P. Silva, J.M.S. Cabral, Cell culture process scale-up challenges for commercial-scale manufacturing of allogeneic pluripotent stem cell products, Bioengineering 9 (3) (2022) 92, http://dx.doi.org/10.3390/bioengineering9030092.

[36] J.A. Thomas, A. Rahman, J. Wutz, Y. Wang, B. DeVincentis, B. McGuire, L. Cao, Modeling free surface gas transfer in agitated lab-scale bioreactors, Chem. Eng. Commun. 210 (8) (2023) 1328–1339, http://dx.doi.org/10.1080/00986445.2022.2084392.

[37] T. Krüger, H. Kusumaatmaja, A. Kuzmin, O. Shardt, G. Silva, E.M. Viggen, The lattice Boltzmann method: principles and practice, in: Graduate Texts in Physics, Springer International Publishing, Cham, 2017, http://dx.doi.org/10.1007/978-3-319-44649-3.

[38] P.-H. Chiu, Y.-T. Lin, A conservative phase field method for solving incompressible two-phase flows, J. Comput. Phys. 230 (1) (2011) 185–204, http://dx.doi.org/10.1016/j.jcp.2010.09.021.

[39] M. Geier, A. Fakhari, T. Lee, Conservative phase-field lattice Boltzmann model for interface tracking equation, Phys. Rev. E 91 (6) (2015) 063309, http://dx.doi.org/10.1103/PhysRevE.91.063309.

[40] J.J.J. Gillissen, H.E.A.V. den Akker, Direct numerical simulation of the turbulent flow in a baffled tank driven by a Rushton turbine, AIChE J. 58 (12) (2012) 3878–3890, http://dx.doi.org/10.1002/aic.13762.

[41] H. Yu, S.S. Girimaji, L.-S. Luo, DNS and LES of decaying isotropic turbulence with and without frame rotation using lattice Boltzmann method, J. Comput. Phys. 209 (2) (2005) 599–616, http://dx.doi.org/10.1016/j.jcp.2005.03.022.

[42] L. Zhu, G. He, S. Wang, L. Miller, X. Zhang, Q. You, S. Fang, An immersed boundary method based on the lattice Boltzmann approach in three dimensions, with application, Comput. Math. Appl. 61 (12) (2011) 3506–3518, http://dx.doi.org/10.1016/j.camwa.2010.03.022.

[43] C. Sirasitthichoke, B. Teoman, J. Thomas, P.M. Armenante, Computational prediction of the just-suspended speed, Njs, in stirred vessels using the lattice Boltzmann method (LBM) coupled with a novel mathematical approach, Chem. Eng. Sci. 251 (2022) 117411, http://dx.doi.org/10.1016/j.ces.2021.117411.

[44] R. Rautenbach, H.M. de León, P. Brorens, M. Schlüter, C. Haringa, Reproducibility of GPU-based large eddy simulations for mixing in stirred tank reactors, Comput. Chem. Eng. 210 (2026) 109615, http://dx.doi.org/10.1016/j.compchemeng.2026.109615.

[45] D.R. Lide, G. Baysinger, S. Chemistry, L.I. Berger, R.N. Goldberg, H.V. Kehiaian, CRC Handbook of Chemistry and Physics, Internet Version 2005, CRC Press, Boca Raton, FL, 2005.

[46] E.M. Schlaich, J.A. Thomas, L. Kandari, G. Tremml, A. Khetan, Experimental and computational characterization of mass transfer in high turndown bioreactors, Biotechnol. Prog. 39 (3) (2023) e3330, http://dx.doi.org/10.1002/btpr.3330.

[47] P. Han, D.M. Bartels, Temperature dependence of oxygen diffusion in H_2 O and D_2 O, J. Phys. Chem. 100 (13) (1996) 5597–5602, http://dx.doi.org/10.1021/jp952903y.

[48] P.P. Brown, D.F. Lawler, Sphere drag and settling velocity revisited, J. Environ. Eng. 129 (3) (2003) 222–231, http://dx.doi.org/10.1061/(ASCE)0733-9372(2003)129:3(222).

[49] T.M. Nijssen, J.T. Padding, M. Ottens, Hydrodynamics of expanded bed adsorption studied through CFD-DEM, Chem. Eng. Sci. 280 (2023) 119027.

[50] S. Hofmann, R. Rautenbach, L. Buntkiel, I.S. Brouwers, L. Gaugler, J. Barczyk, J. Fitschen, S. Reinecke, M. Hoffmann, R. Takors, U. Hampel, M. Schlüter, Lagrangian sensor particles for detecting hydrodynamic heterogeneities in industrial bioreactors: experimental analysis and lattice-Boltzmann simulations, Chem. Eng. J. Adv. 22 (2025) 100744, http://dx.doi.org/10.1016/j.ceja.2025.100744.

[51] B. Blais, O. Bertrand, L. Fradette, F. Bertrand, CFD-DEM simulations of early turbulent solid–liquid mixing: prediction of suspension curve and just-suspended speed, Chem. Eng. Res. Des. 123 (2017) 388–406, http://dx.doi.org/10.1016/j.cherd.2017.05.021.

[52] J.J. Chalmers, Mixing, aeration and cell damage, 30+ years later: What we learned, how it affected the cell culture industry and what we would like to know more about, Curr. Opin. Chem. Eng. 10 (2015) 94–102, http://dx.doi.org/10.1016/j.coche.2015.09.005.

[53] A. Anand, M. McCahill, J. Thomas, A. Sood, J. Kinross, A. Dasgupta, A. Rajendran, An *in-silico* analysis of hydrodynamics and gas mass transfer characteristics in scale-down models for mammalian cell cultures, J. Biotech. 388 (2024) 96–106, http://dx.doi.org/10.1016/j.jbiotec.2024.04.013.

[54] T.N. Zwietering, Suspending of solid particles in liquid by agitators, Chem. Eng. Sci. 8 (3) (1958) 244–253, http://dx.doi.org/10.1016/0009-2509(58)85031-9.

[55] G. Micale, F. Grisafi, A. Brucato, Assessment of particle suspension conditions in stirred vessels by means of pressure gauge technique, Chem. Eng. Res. Des. 80 (8) (2002) 893–902, http://dx.doi.org/10.1205/026387602321143444.

[56] S. Pirker, D. Kahrimanovic, C. Goniva, Improving the applicability of discrete phase simulations by smoothening their exchange fields, Appl. Math. Model. 35 (5) (2011) 2479–2488, http://dx.doi.org/10.1016/j.apm.2010.11.066.

[57] A. Zhang, V.L. Tsang, R. Korke-Kshirsagar, T. Ryll, Effects of pH probe lag on bioreactor mixing time estimation, Process Biochem. 49 (6) (2014) 913–916, http://dx.doi.org/10.1016/j.procbio.2014.03.005.

[58] K. van 't Riet, R.G.J.M. van der Lans, Mixing in bioreactor vessels, in: Mixing in Bioreactor Vessels, Academic Press, 2011, pp. 63–80.

[59] K. Van't Riet, Review of measuring methods and results in nonviscous gas-liquid mass transfer in stirred vessels, Ind. Eng. Chem. Process. Des. Dev. 18 (3) (1979) 357–364, http://dx.doi.org/10.1021/i260071a001.

[60] H. Zhu, A.W. Nienow, W. Bujalski, M.J.H. Simmons, Mixing studies in a model aerated bioreactor equipped with an up- or a down-pumping 'elephant ear' agitator: power, hold-up and aerated flow field measurements, Chem. Eng. Res. Des. 87 (3) (2009) 307–317, http://dx.doi.org/10.1016/j.cherd.2008.08.013.

[61] A.W. Nienow, Hydrodynamics of stirred bioreactors, Appl. Mech. Rev. 51 (1) (1998) 3–32, http://dx.doi.org/10.1115/1.3098990.

[62] T.M.J. Nijssen, H.A.M. Kuipers, J. van der Stel, A.T. Adema, K.A. Buist, Complete liquid-solid momentum coupling for unresolved CFD-DEM simulations, Int. J. Multiph. Flow 132 (2020) 103425, http://dx.doi.org/10.1016/j.ijmultiphaseflow.2020.103425.

[63] M.S. Croughan, J.-F. Hamel, D.I.C. Wang, Hydrodynamic effects on animal cells grown in microcarrier cultures, Biotechnol. Bioeng. 29 (1) (1987) 130–141, http://dx.doi.org/10.1002/bit.260290117.

[64] S. Hofmann, C. Weiland, J. Fitschen, A. von Kameke, M. Hoffmann, M. Schlüter, Lagrangian sensors in a stirred tank reactor: comparing trajectories from 4D-particle tracking velocimetry and lattice-Boltzmann simulations, Chem. Eng. J. 449 (2022) 137549, http://dx.doi.org/10.1016/j.cej.2022.137549.

[65] A.P. Grima, P.W. Wypych, Investigation into calibration of discrete element model parameters for scale-up and validation of particle–structure interactions under impact conditions, Powder Technol. 212 (1) (2011) 198–209, http://dx.doi.org/10.1016/j.powtec.2011.05.017.

[66] G.K.P. Barrios, R.M. de Carvalho, A. Kwade, L.M. Tavares, Contact parameter estimation for DEM simulation of iron ore pellet handling, Powder Technol. 248 (2013) 84–93, http://dx.doi.org/10.1016/j.powtec.2013.01.063.

[67] H.Q. Do, A.M. Aragón, D.L. Schott, A calibration framework for discrete element model parameters using genetic algorithms, Adv. Powder Technol. 29 (6) (2018) 1393–1403, http://dx.doi.org/10.1016/j.apt.2018.03.001.

[68] P. Jüsten, G.C. Paul, A.W. Nienow, C.R. Thomas, Dependence of mycelial morphology on impeller type and agitation intensity, Biotechnol. Bioeng. 52 (6) (1996) 672–684, http://dx.doi.org/10.1002/(SICI)1097-0290(19961220)52:6<672::AID-BIT5>3.0.CO;2-L.

[69] C. Bratengeier, A. Liszka, J. Hoffman, A.D. Bakker, A. Fahlgren, High shear stress amplitude in combination with prolonged stimulus duration determine induction of osteoclast formation by hematopoietic progenitor cells, FASEB J. 34 (3) (2020) 3755–3772, http://dx.doi.org/10.1096/fj.201901458R.